Grain boundary-engineered La_2CuO_4 perovskite nanowires for efficient CO_2 reduction reaction

Juan Wang,[†,‡] Chen Cheng,[§] Bolong Huang,[‼] Jianlei Cao,[‡] Leigang Li,[‡] Qi Shao,[‡] Liang Zhang,[§] and Xiaoqing Huang[,†]*

[†]College of Chemistry and Chemical Engineering, Xiamen University, Xiamen, 361005, China.

[‡]College of Chemistry, Chemical Engineering and Materials Science, Soochow University, Jiangsu, 215123, China.

[§]Institute of Functional Nano & Soft Materials (FUNSOM), Jiangsu Key Laboratory for Carbon-Based Functional Materials and Devices, Soochow University, Jiangsu, 215123, China.

[‼]Department of Applied Biology and Chemical Technology, The Hong Kong Polytechnic University, Hung Hom, Kowloon, Hong Kong SAR, China.

E-mail: hxq006@xmu.edu.cn

Abstract: Electroreduction of carbon dioxide (CO_2) has been regarded as a promising approach to realize the production of useful fuels and decrease of the green-house gas level simultaneously, whereas high-efficiency catalysts are required to achieve this goal. Herein, we create a series of La_2CuO_4 perovskites with modulated grain boundaries as efficient electrocatalysts for CO_2 reduction. The La_2CuO_4 nanobamboos (La_2CuO_4 NBs) with rich twin boundaries show a high Faraday efficiency (FE) of 60% towards ethylene (C_2H_4) synthesis, while bulk La_2CuO_4 exhibits a FE of 91% towards CO generation. X-ray absorption spectroscopy (XAS) reveals that the Cu in La_2CuO_4 NBs is in an unsaturated Cu^{2+} state, which can improve the adsorption of intermediate species to enhance FE_{C2H4}. No obvious change can be

observed before and after the catalytic reaction as well as during the catalytic process as revealed by the *in situ* XAS studies. Density functional theory calculations reveal that the superior performances of La_2CuO_4 NBs towards CO_2RR originate from the active (113) surfaces with intrinsic strain. The formation of gap states in (113) surface annihilates the electron transfer barrier of C-C coupling for C_2 products, which is responsible for achieving the high FE of C_2H_4 over La_2CuO_4 NBs. This work provides a new perspective for developing efficient perovskite catalysts via grain boundary engineering.

Keywords: La_2CuO_4 perovskite • Nanowire • Twin boundary • Ethylene • CO_2 reduction

Electrochemical reduction of carbon dioxide (CO_2) into value-added chemicals and fuels is of paramount significance for alleviating the serious environmental issues and energy crisis.[1-4] Up to date, high Faraday efficiency (FE) for C_1 products (i.e., carbon monoxide and formate) has been realized over many electrocatalysts by CO_2 reduction reaction (CO_2RR).[5-9] However, the efficient production of highly value-added C_2 products (i.e., ethylene and ethanol) via CO_2RR still faces enormous challenges due to the complex electron transfer process and poor selectivity.[10, 11] Since copper (Cu) was discovered to have the unique ability to produce hydrocarbons by Shin *et al.*, a substantial amount of Cu-based materials have been designed and employed as electrocatalysts for CO_2RR, but the inferior corrosion resistance, low FE and the nature of being easily reduced limit their further applications.[12-15] Therefore, developing unique Cu-based electrocatalysts for producing hydrocarbons at high FE and selectivity is extemely desired.

To enhance the selectivity of hydrocarbon, diversified strategies, including crystal plane control, construction of core-shell nanostructures and reconstruction of the ensemble of nanoparticles, have been proposed to tune the energetics of intermediate species on catalysts during CO_2RR.[16-18] Unfortunately, the

FE of these electrocatalysts is still unsatisfactory because the weak adsorption of the CO intermediate on the active site makes it difficult to promote C-C coupling.[19] To this end, regulating electronic structures and creating coordinatively unsaturated environment for enhanced interaction between intermediate species and catalysts would be a potential way of obtaining highly efficient electrocatalysts for CO_2RR. Perovskites are widely used as catalysts for electrochemical conversion of H_2O, NO_x and CO due to their chemical versatility, easy regulation of electronic and crystal structure, earth-abundancy and low cost.[20-23] For example, Zeng, *et al.* provided an effective strategy to modify the electronic structure of $LaCoO_3$ perovskite for achieving a highly active OER electrocatalyst by varying the particle size.[24] Although great progress has been achieved, expanding their application scope of perovskites, such as CO_2RR, remains a significant goal for solving environment problems and energy shortages.[25, 26] $SrSnO_3$ perovskite nanowires were reported to catalyze the conversion of CO_2 to formate.[27] However, the lack of C-C coupling capacity makes it impossible to obtain high-energy-density hydrocarbon products. Therefore, designing and constructing unique Cu-based perovskite electrocatalysts for CO_2RR is attractive yet challenging.

Here we present a series of La_2CuO_4 perovskites with modulated grain boundaries, where La_2CuO_4 NBs show a fairly high FE_{C2H4} of 60%, surpassing many reported Cu-based electrocatalysts, while bulk La_2CuO_4 achieves a FE of up to 91% towards CO generation. X-ray absorption spectroscopy (XAS) analysis reveals that the presence of strain at twin boundaries (TBs) can increase the bond length of Cu-O and Cu-La, and create a coordinatively unsaturated environment, resulting in improved intermediate adsorption and thus enhanced FE_{C2H4}. It is worth mentioning that the changes of the La_2CuO_4 NBs before and after the catalytic reaction or during the catalytic process are negligible as comfirmed by the *in situ* XAS monitoring. Density functional theory (DFT) calculations have unraveled the distinct activities of (113) and (111) surfaces of La_2CuO_4, which gives rise to the different CO_2RR reduction products and FEs. The highly electroactive (113) surface with the facilitation of strain dominates the efficient reduction of

CO_2 to C_2H_4. This work provides a new insight for constructing efficient perovskite catalysts with coordinatively unsaturated environment for CO_2RR and beyond.

Results. The La_2CuO_4 NBs perovskites were prepared by electrospinning followed by calcination at 700 °C for 2 h under air atmosphere (**Figure 1a**). The initial electrospun naofibers exhibit interconnected three-dimensional (3D) network structure with smooth surface (**Figure S1**). The heating rate was found to have significant influence to the surface morphology of La_2CuO_4. Interestingly, nanobamoos (NBs) morphology was observed by simply tuning the heating rate to 1 °C/min during calculation processs. Contrary to the initial smooth surface, the calcinated La_2CuO_4 NBs exhibit rugged surface and still remain the 3D network structure (**Figure 1b** and **Figure S2a**). Transmission electron microscopy (TEM) images reveal that the La_2CuO_4 NBs consist of a series of single grain connected by distinct grain boundaries (GBs), forming a bamboo-like morphology (**Figure 1c** and **Figure S2b**). The atomic ratio of La/Cu is about 2:1, as determined by scanning electron microscopy energy-dispersive X-ray spectroscopy (SEM-EDS) and inductively coupled plasma atomic emission spectrometry (ICP-AES) (**Figure S3** and **Table S1**). It is found that the elements of La, Cu and O distribute homogeneously on the La_2CuO_4 NBs, as revealed by the STEM-EDS elemental mappings (**Figure 1d**). To investigate the strucutre and phase of La_2CuO_4 NBs, powder X-ray diffraction (PXRD) analysis was performed. As shown in **Figure 1e**, all the diffraction peaks match well with orthorhombic-type perovskites of La_2CuO_4 with a space group of *Fmmm*. The crystal structure of La_2CuO_4 is displayed in **Figure 1f,** where the CuO_6 octahedra regularly locate in the structure and La atoms are inserted into octahedral space. The unit cell parameter was obtained from PXRD by using the Rietveld refinement (**Table S2**). For comparison, La_2CuO_4 nanorods (La_2CuO_4 NRs) and bulk La_2CuO_4 were obtained by tuning the heating rate from 1 °C/min to 5 °C/min and 10 °C/min,

respectively. (**Figure S4-6**). Compared with La_2CuO_4 NBs, the length of La_2CuO_4 NRs is shorter and the 3D network structure is destroyed because the higher heating rate during the calcination process results in fracture of nanostructure. As revealed by TEM image of La_2CuO_4 NRs, single grains are randomly arranged. The GBs of La_2CuO_4 NRs are obviously different from these of La_2CuO_4 NBs. For bulk La_2CuO_4, single grains of various sizes stack disorderly with no distinct grain boundaries. SEM-EDS, ICP-AES, STEM-EDS elemental mapping and PXRD analysis of La_2CuO_4 NRs and bulk La_2CuO_4 show similar results to those of La_2CuO_4 NBs, indicating that the heating rate only changes the morphology and grain boundaries without affecting their chemical compositions and crystalline structures.

To investigate the formation process of La_2CuO_4 NBs, thermal gravimetric (TG) and corresponding derivate thermogravimetry (DTG) curve were collected and shown in **Figure S7**. Apparently, two significant weight losses occurred at 100 °C and 300 °C, respectively. The two weight losses are attributed to the evaporation of moisture and residual solvent as well as the decomposition of PVP and nitrate, respectively, being consistent with the results of fourier transform infrared (FTIR) spectroscopy (**Figure S8**).[28, 29] It is speculated that the pure perovskite nanofibers are fully formed when the temperature reaches 600 °C because no further mass loss ocuurs. To verify this conjecture, detailed characterizations were further carried out. Apparently, a small amount of nanoparticles will precipitate on the smooth surface of the nanofibers as the temperture increases. Subsequently, the nanopartciles disappear and the surface of the nanofibers becomes rough. The bamboo-like morphology is formed once the temperature reaches 600 °C (**Figure S9-14**). However, this unique structure and morphology can be destroyed at higher tempertures (**Figure S15**). PXRD analysis shows that the intensity of diffraction peaks gradually increases with the increase of temperature, indicating enhanced crystallinity. The perovskite phase starts to be formed when the temperature reaches 400 °C and pure perovskite phase is obtained at 600 °C (**Figure S16**). The calcination treatment only affects the morphology and phase, but has hardly influence to the

composition (**Figure S17**).

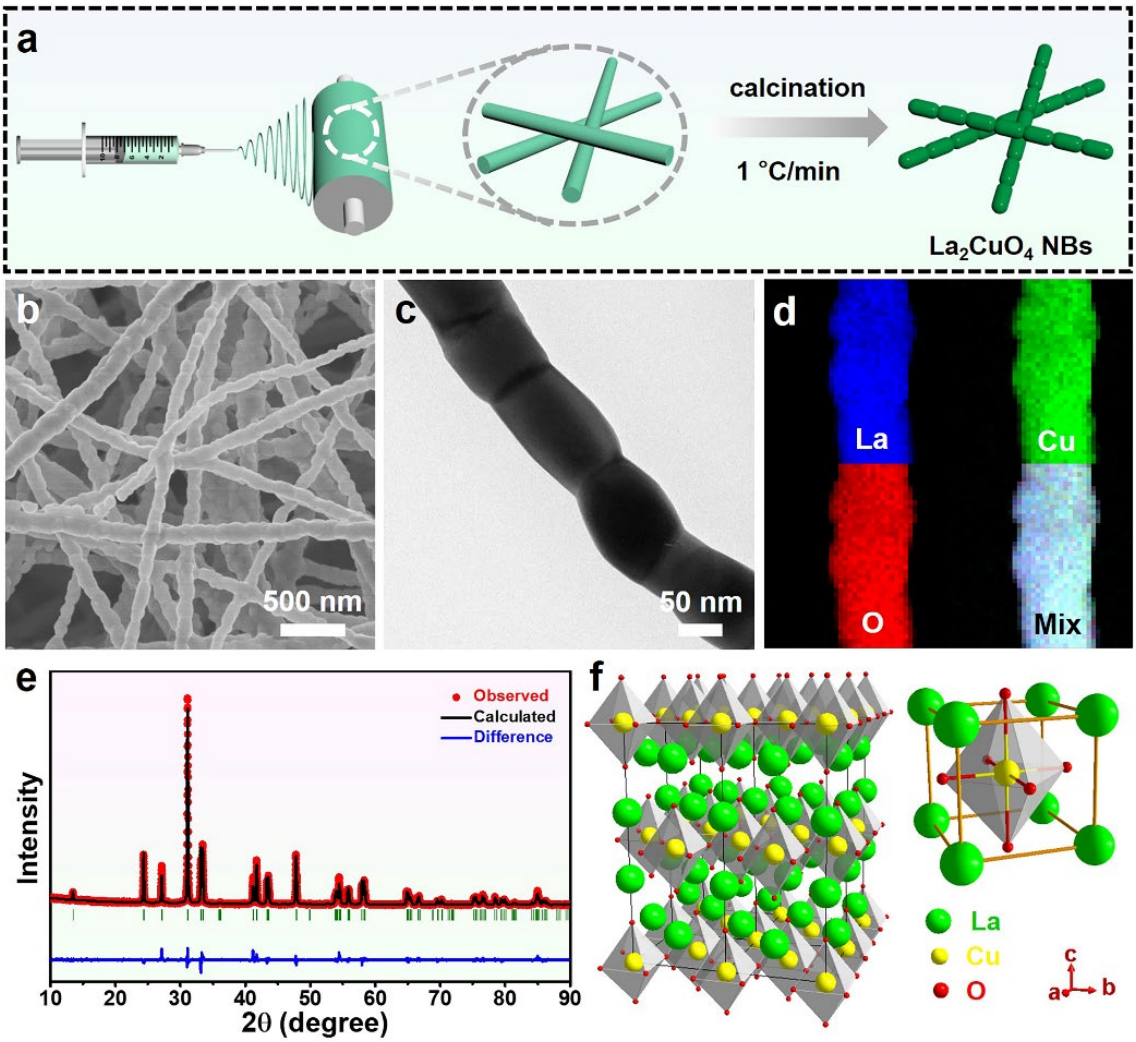

Figure 1. (**a**) Schematic illustration of synthetic process of La_2CuO_4 NBs. (**b**) SEM image, (**c**) TEM image, (**d**) STEM-EDS elemental mappings, (**e**) PXRD pattern and (**f**) crystal model of La_2CuO_4 NBs.

Considering the different morphologies and grain boundaries of La_2CuO_4 perovskites, the type and structure of grain boundaries were carefully investigated. As schematically shown in **Figure 2a**, TBs are formed by planar defects separated by the twin plane, where the arrangement of atoms on both sides is mirror symmetrical. On the other hand, ordinary GBs are interfaces formed by planar defects in which atoms on both sides are arranged randomly, as shown in **Figure 2b**. Atoms tend to be in a regular arrangement in the absence of GBs (**Figure 2c**). As GBs are observed in La_2CuO_4 NBs and La_2CuO_4 NRs,

high-resolution TEM (HRTEM) analysis was conducted to further explore the type of GBs. TBs were clearly observed at the bamboo joints of La_2CuO_4 NBs and the angle between the two sides of the TBs is 124° (**Figure 2d**). Interestingly, compared with the interplanar spacing (0.288 nm) of (113) facet, the different interplanar spacing (0.297 nm and 0.285 nm) of (113) facets on both sides of TBs indicates that one side of the TB is stretched and the other side is compressed, demonstrating the existence of strain at TBs (**Figure S18**). Fast Fourier transforms (FFTs) for La_2CuO_4 NBs on both sides of TBs were obtained and the different patterns of FFTs indicate the deformation of crystal facets on both sides of TBs. With respective to La_2CuO_4 NRs, many GBs are observed. As revealed in **Figure 2e** and **Figure S19**, (113) facet with an interplanar spacing of 0.288 nm is observed on one side of GBs and (111) facet with a crystalline interplanar spacing of 0.366 nm is revealed on the other side. The FFTs patterns on both sides of GBs are different, further demonstrating different crystal planes on both sides of GBs. **Figure 2f** shows the HRTEM of bulk La_2CuO_4 and distinct lattice fringes are observed, where interplanar spacing of 0.288 nm is ascribed to that of (113) facet and interplanar spacing of 0.366 nm is ascribed to that of (111) planar of La_2CuO_4 perovskite. No GBs exist in bulk La_2CuO_4 and areas A and B in Figure 2f exhibit the different FFTs patterns.

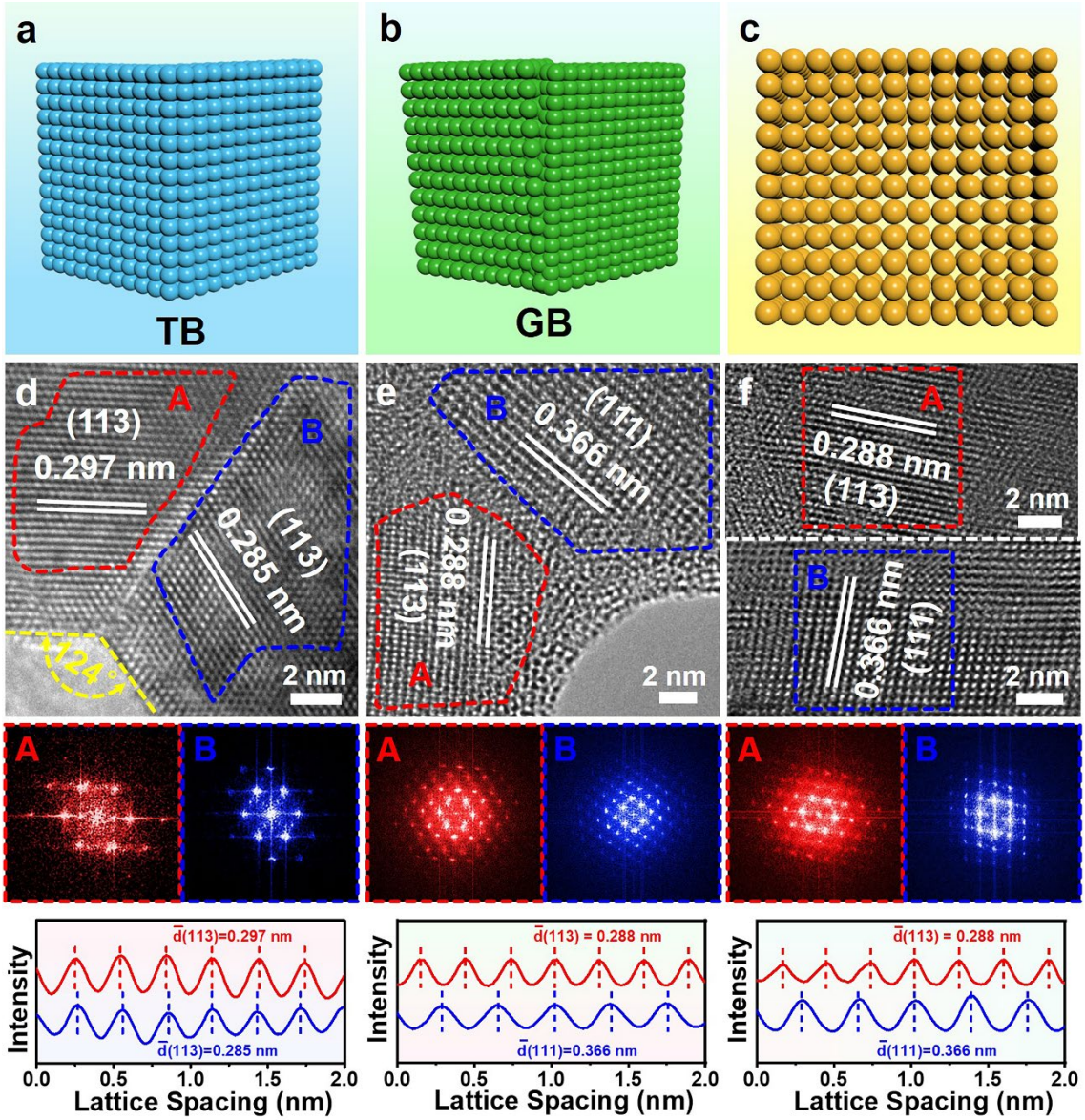

Figure 2. (**a-c**) Schematic illustration of different grain boundaries. HRTEM images of (**d**) La_2CuO_4 NBs, (**e**) La_2CuO_4 NRs and (**f**) bulk La_2CuO_4. Corresponding FFTs of A (red dashed box) and B (blue dashed box) areas are shown below. Intensity profiles taken along the atomic layers from A and B areas in (d-f).

The catalytic performance of the three La_2CuO_4 perovskites towards CO_2RR was investigated. We perform linear sweep voltammetry (LSV) measurements for these catalysts in a CO_2-saturated 0.1 M $KHCO_3$ electrolyte using an H-type cell, where bulk La_2CuO_4 exhibits the strongest current response (**Figure S20**). Chronoamperometry measurements were carried out in a CO_2-saturated 0.1 M $KHCO_3$

solution for 2 h to reduce CO_2, and the gas products were quantified by gas chromatography while liquid products were analyzed by nuclear magnetic resonance (NMR) spectroscopy (**Figure S21-24**). The histogram of product FE for the three La_2CuO_4 perovskites at various applied potentials are shown in **Figure 3**. It is worth noting that La_2CuO_4 NBs, La_2CuO_4 NRs and bulk La_2CuO_4 exhibit significantly different selectivity toward C_1 and C_2 products, indicating that the GBs play a crucial role in influencing the obtained products of CO_2RR. Significantly, La_2CuO_4 NBs show a fairly high FE_{C2H4} of 60 % at -1.0 V versus reversible hydrogen evolution electrode (vs. RHE), surpassing those of most reported Cu-based CO_2RR electrocatalysts (**Figure 3a** and **Table S3**). La_2CuO_4 NRs show lower FE_{C2H4} and higher FE_{H2} than that of La_2CuO_4 NBs at all applied potentials (**Figure 3b**). For bulk La_2CuO_4, no C_2H_4 was detected during the CO_2RR process. Interestingly, CO FE of up to 91% was obtained for bulk La_2CuO_4 at -1.0 V vs. RHE (**Figure 3c**). To further investigate product variation of these La_2CuO_4 perovskites, the FE of major products at the same potential of -1.0 V was compared. As shown in **Figure 3d**, La_2CuO_4 NBs exhibit the highest FE_{C2H4} of 60%, which is 4.8 times of that of La_2CuO_4 NRs (12.4%), while no ethylene was detected for bulk La_2CuO_4 NRs. With respect to CO production, bulk La_2CuO_4 shows the highest FE_{CO} of 91%, which was 8.2 and 20.2 times of those of La_2CuO_4 NRs (11.1%) and La_2CuO_4 NBs (4.5%), respectively. Subsequently, chronoamperometry measurements were performed on La_2CuO_4 NBs and bulk La_2CuO_4 to evaluate their CO_2RR stabilities. As shown in **Figure 3e**, the total geometric current density of both catalysts remains stable for up to 12 h during the stability test and only subtle fluctuation was observed for the FE_{C2H4} of La_2CuO_4 NBs and the FE_{CO} of bulk La_2CuO_4. To investigate the variation of La_2CuO_4 NBs during CO_2RR, detailed characterizations were carried out after chronoamperometry test. As shown in **Figure S25**, La_2CuO_4 NBs still keep the 3D interconnected network with TBs. PXRD pattern, SEM-EDS spectrum and STEM-EDS elemental mappings show that the crystal structure, atomic ratio and element distribution are largely maintained, indicating the high stability of La_2CuO_4 NBs during CO_2RR.

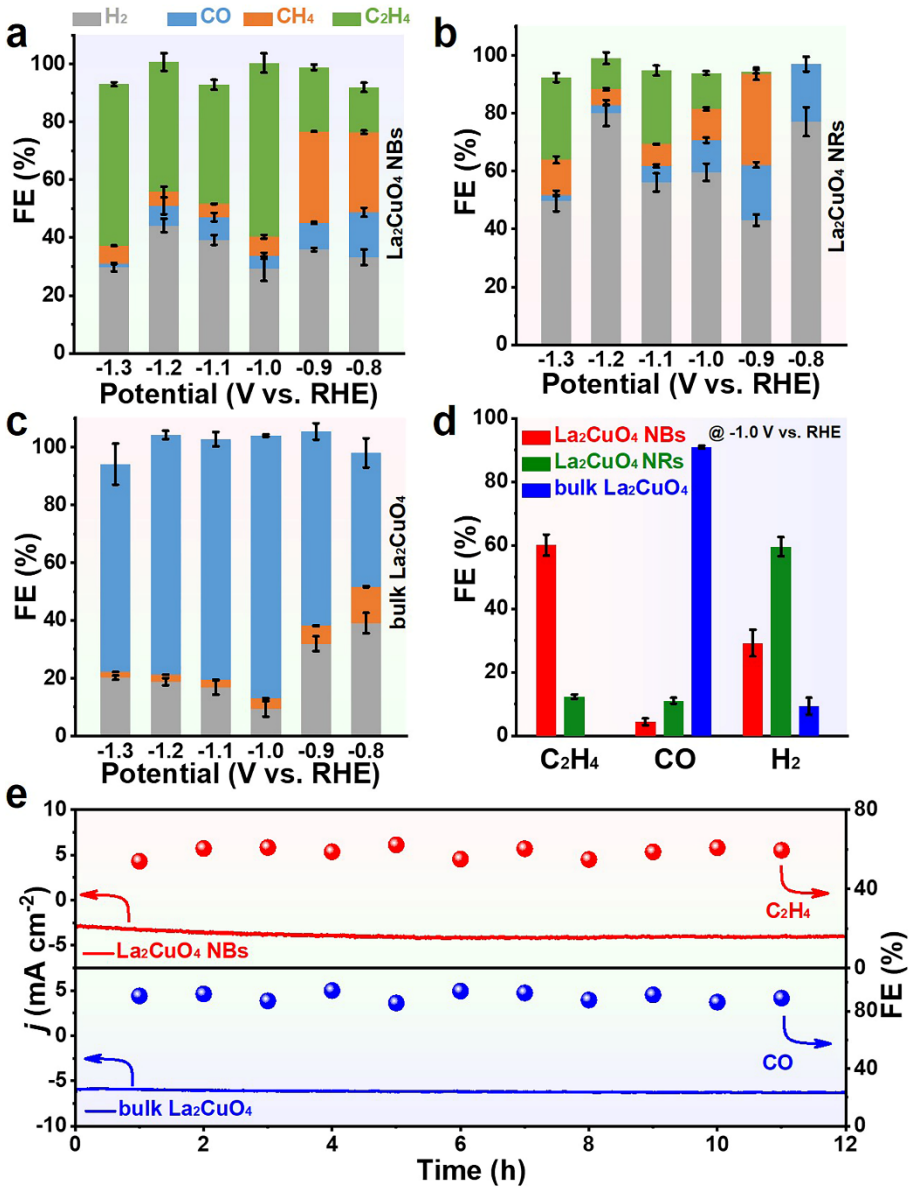

Figure 3. Faradaic efficiencies of (**a**) La_2CuO_4 NBs, (**b**) La_2CuO_4 NRs and (**c**) bulk La_2CuO_4 at different potentials. (**d**) Histograms of C_2H_4, CO and H_2 Faradaic efficiencies for La_2CuO_4 NBs, La_2CuO_4 NRs and bulk La_2CuO_4 at -1.0 V vs. RHE. (**e**) Stability test for C_2H_4 and CO production over La_2CuO_4 NBs and bulk La_2CuO_4.

Discussion. Since electrochemical CO_2RR generally occurs at the gas-solid-liquid three-phase interface, the adsorption of CO_2 on the catalyst is a critical prerequisite. To investigate the interaction between the catalyst and CO_2, CO_2 temperature-programmed desorption (TPD) measurement was carried out. As

shown in **Figure 4a**, La_2CuO_4 NRs shows the weakest adsorption of CO_2 as the temperature of CO_2 chemical desorption peak is the lowest among the three catalysts, leading to low activity towards CO_2RR, which is consistent with the experimental results. In addition, bulk La_2CuO_4 exhibits a distinct CO_2 desorption peak in a wide high-temperature range, indicating higher CO_2 adsorption capacity.[30] Electrolyzing CO_2 to CO intermediate and maintaining strong binding energy of CO on the active site is significant for promoting C-C coupling during CO_2RR process. To this end, CO-TPD was further used to evaluate the adsorption behavior of CO on catalyst (**Figure 4b**), where the lowest temperature of CO adsorption peak of bulk La_2CuO_4 among these catalysts indicates the strong desorption ability of CO-realted intermediates, and consequently, CO is the main detected product.[31] The significant increase in CO desorption peak temperature indicates a stronger adsorption affinity for CO-related intermediates on La_2CuO_4 NBs and La_2CuO_4 NRs, explaining the enhanced selectivity of C_2H_4. Considering the different binding capabilities for CO_2 and CO, the coordination environment and local atomic structure were analyzed by XAS. Apparently, the feature and position of Cu L-edge soft X-ray absorption fine structure (XANES) spectra for La_2CuO_4 perovskites are similar to that of standard CuO, and no obvious signal of Cu^0 and Cu^+ can be observed. The results were also confirmed by Cu K-edge XANES spectra, demonstrating that the Cu in all catalysts is in the state of Cu^{2+} (**Figure 4c** and **Figure S26**). The Fourier transform of Cu K-edge extended X-ray absorption fine structure (EXAFS) shows that the peaks of La_2CuO_4 NBs, La_2CuO_4 NRs and bulk La_2CuO_4 are around about 1.9 Å, attributed to the Cu-O bonds (**Figure 4d**). Compared with standard CuO, obvious peaks of La_2CuO_4 NBs, La_2CuO_4 NRs and bulk La_2CuO_4 at about 3.2 Å can be assigned to the Cu-La bonds. Likewise, no Cu-Cu bonds can be observed for all catalysts, consistent with the results of XANES. To accquire detailed structure information, the EXAFS spectra were fitted and the results are summarized (**Figure S27** and **Table S4**). In detail, the coordination number of Cu-O and Cu-La in La_2CuO_4 NBs are 2.05 and 7.18, respectively, which are

significantly smaller than those of La_2CuO_4 NRs (3.20 and 10.10) and bulk La_2CuO_4 (3.20 and 9.91). Compared with La_2CuO_4 NRs and bulk La_2CuO_4, slight increase of Cu-O and Cu-La bond length can be observed for La_2CuO_4 NBs, demonstrting that the presence of strain in TBs, which was comfirmed by the results of HRTEM. Based on the above analysis, it is propsoed that the presence of strain in TBs will increase the bond length of Cu-O and Cu-La and create a coordinatively unsaturated environment, resulting in improved intermediate adsorption and enhanced FE_{C2H4}. The wavelet spectra of La_2CuO_4 NBs, La_2CuO_4 NRs and bulk La_2CuO_4 contain two distinc intensity of Cu-O and Cu-La coordination, consistent with the curve-fitting results (**Figure 4e** and **Figure S28**). To evaluate the evolution of La_2CuO_4 NBs during the electrocatalytic process, *in situ* XANES spectra were also conducted under the measurement conditions (**Figure 4f**). Obviuosly, the Cu K-edge XANES spectrum of La_2CuO_4 NBs at open circuit potential in CO_2 saturated 0.1 M $KHCO_3$ solution shows a similar outline and position to that of the conventional test, indicating that the electrolyte and CO_2 do not change the valence state of the catalyst. Interestingly, the Cu K-edge XANES spectrum is still well maintained when a voltage of -1.0 V vs. RHE was applied. The above results demonstrte that the catalyst is relatively stable before and after the catalytic reaction or during the catalytic process, which can also be confirmed by Cu L-edge soft XANES spectra (**Figure S29**).

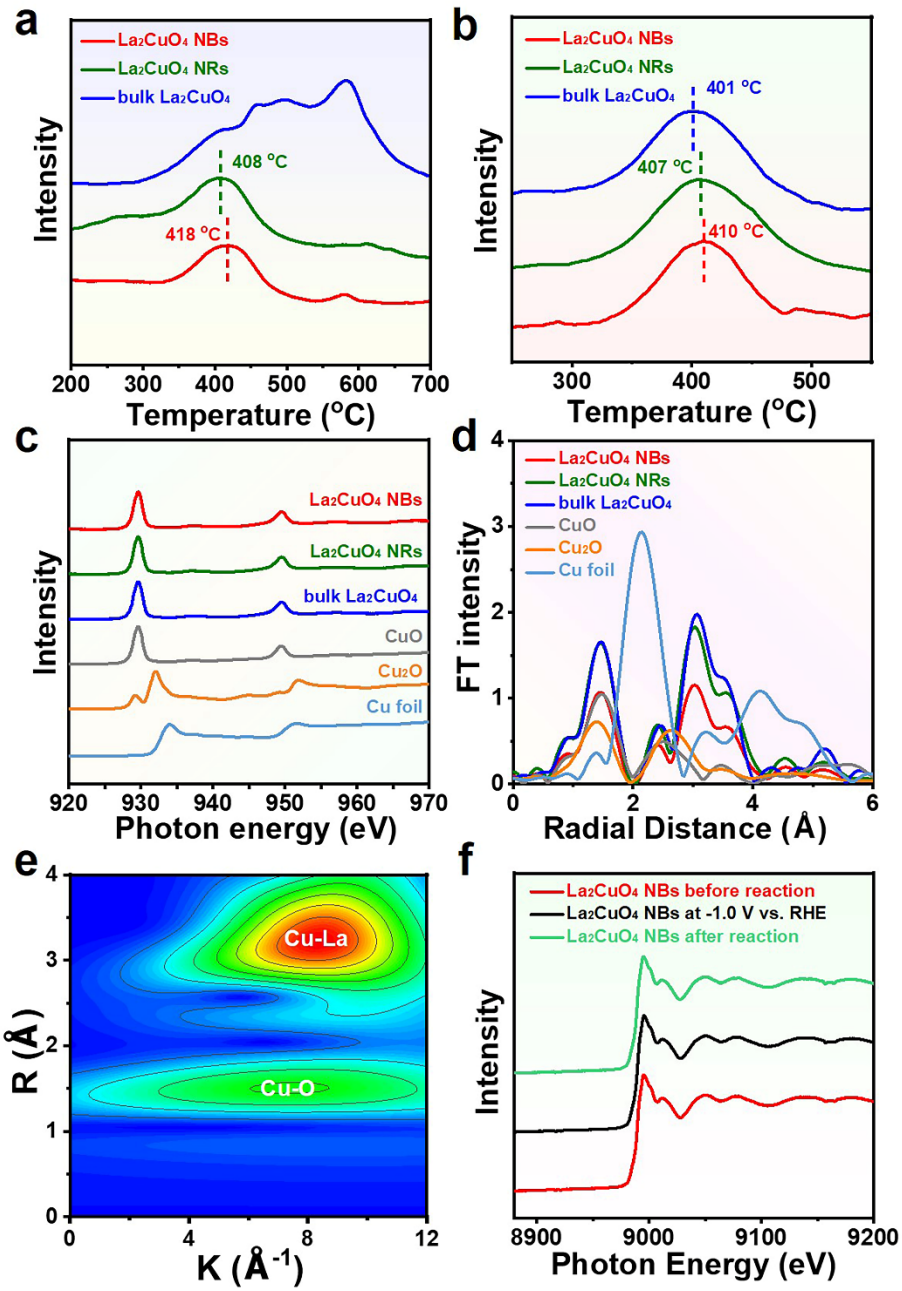

Figure 4. (a) CO_2 and (b) CO TPD profiles of La_2CuO_4 NBs, La_2CuO_4 NRs and bulk La_2CuO_4. (c) Cu L-edge XANES and (d) Cu K-edge EXAFS spectra of La_2CuO_4 NBs, La_2CuO_4 NRs, bulk La_2CuO_4, standard CuO, Cu_2O and Cu foil. (e) Wavelet transform of Cu K-edge EXAFS data of La_2CuO_4 NBs. (f) In situ Cu K-edge XANES spectra of La_2CuO_4 NBs at -1.0 V vs. RHE and open circuit before and after reaction.

DFT calculations are applied to explore the origins of high performances of CO_2 reduction on the La_2CuO_4 NBs. We have constructed the curvature boundary of three different material systems including the (113)

twin boundary, the (111) twin boundary, and (113)/(111) boundary (**Figure S30a-c**). It is noted that the (113) TB easily form the curvature boundary with subtle lattice mismatch. Meanwhile, both (111) TB and (113)/(111) GB show some mismatch bonding at the interface due to the lattice mismatch during the formation of curvature structure. Therefore, we have compared the stabilization energy of these structures (**Figure S30d**). (113) TB shows the most stable structure with the lowest energy of -1.30 eV while the (113)/(111) GB demonstrates the highest energy of -1.00 eV, supporting the higher instability of GB than TB. These results confirm that the formation of TB leads to a more stable nanostructure of La_2CuO_4 NBs, which is critical for stable and efficient electrocatalysis. The corresponding adsorption energies of the CO_2 on different surfaces have been compared. For the (113) TB, the adsorption of CO_2 prefers the (113) surface sites than the boundary region (**Figure S30e**). In the (113)/(111) GB surface, the surface still shows the more preferred adsorption of CO_2 on the (113) surface side than the (111) surface and the GB region. Meanwhile, the (113) TB also shows overall lower adsorption energies of CO_2, supporting a more energetically preferred CO_2 reduction on the La_2CuO_4 NBs with abundant twin boundaries. In the end, we also consider the strain effect induced in the TB boundary, which has also been confirmed by the EXAFS results (**Figure S30f**). With the tensile strain, we notice that the adsorption energies of CO_2 and the energy of CO-CO coupling are both further lowered. Such trends facilitate both the efficiency of CO_2RR as well as the selectivity towards the C_2 product.

For a more detailed look, both surfaces of (113) and (111) are investigated regarding both electronic environment and energetic physicochemical trend. For the (113) surfaces, the bonding and anti-bonding orbitals near Fermi level (E_F) demonstrate the highly electroactive region dominantly concentrates on the surface Cu sites. We also identify the existence of gap states near La sites and O sites (**Figure 5a**). For the (111) surfaces, the Cu site is still playing as the electroactive region while the gap states become narrower than that of (113) surfaces. The evidently different electronic distribution indicates the distinct selectivity

of the surface for the CO_2 reduction (**Figure 5b**). By a further look into the partial projected density of states (PDOSs), the different subtle electronic structure is revealed. For (113) surface, Cu-3d orbitals display a sharp peak near EV-1.5 eV (EV = 0 eV) while the O-2p orbitals exhibit a broad coverage from EV to EV-6.0 eV. The main contribution of La-5d orbitals lies in the conduction band. Notably, the gap states are constructed by the joint contribution of La, Cu, and O sites, which significantly promote the electron transfer by the annihilation of the barriers (**Figure 5c**). Although the electronic contribution on (111) surface also shows the main contribution of Cu and La for both valence band maximum (VBM) and conduction band minimum (CBM), respectively, the electron transfer barrier still exists, which cannot be alleviated by the gap states. Such a barrier determines the electron transfer efficiency on (111) surface is consequently much lowered, especially for the C-C coupling. The strain induced in the interfacial region of La_2CuO_4 NBs and La_2CuO_4 NRs facilitates the electron transfer, which explains only C_1 product is obtained for bulk La_2CuO_4 (**Figure 5d**). For the complicated C_2 route of CO_2 reduction, the PDOSs of the key adsorbates are also illustrated. On (113) surface, from the adsorption of the initial reactant to the final product C_2H_4, we notice a linear correlation on the dominant peak of the in the PDOSs, which guarantees the efficient electron transfer in the reaction coordinates. Meanwhile, Cu-3d orbitals demonstrate a highly stable valence state, which is consistent with the experiment characterizations (**Figure 5e**). On the contrary, such a linear correlation has been obviously weakened in (111) surfaces, which is attributed to the C-C coupling with a larger electron transfer barrier induced by the overbinding of CO. In addition, a slight downshifting of the Cu-3d band center has been noticed, indicating the local electroactivity on the surface is affected by the adsorption of intermediates (**Figure 5f**). By comparing the PDOS of both adsorbed CO, (113) surface shows a more evident reduction trend due to the larger downshifting of CO orbitals, facilitating the further C-C coupling. Meanwhile, the (111) surface demonstrates the stronger electron transfer with proton, which leads to the high production of H_2 as the experimental results (**Figure 5g**).

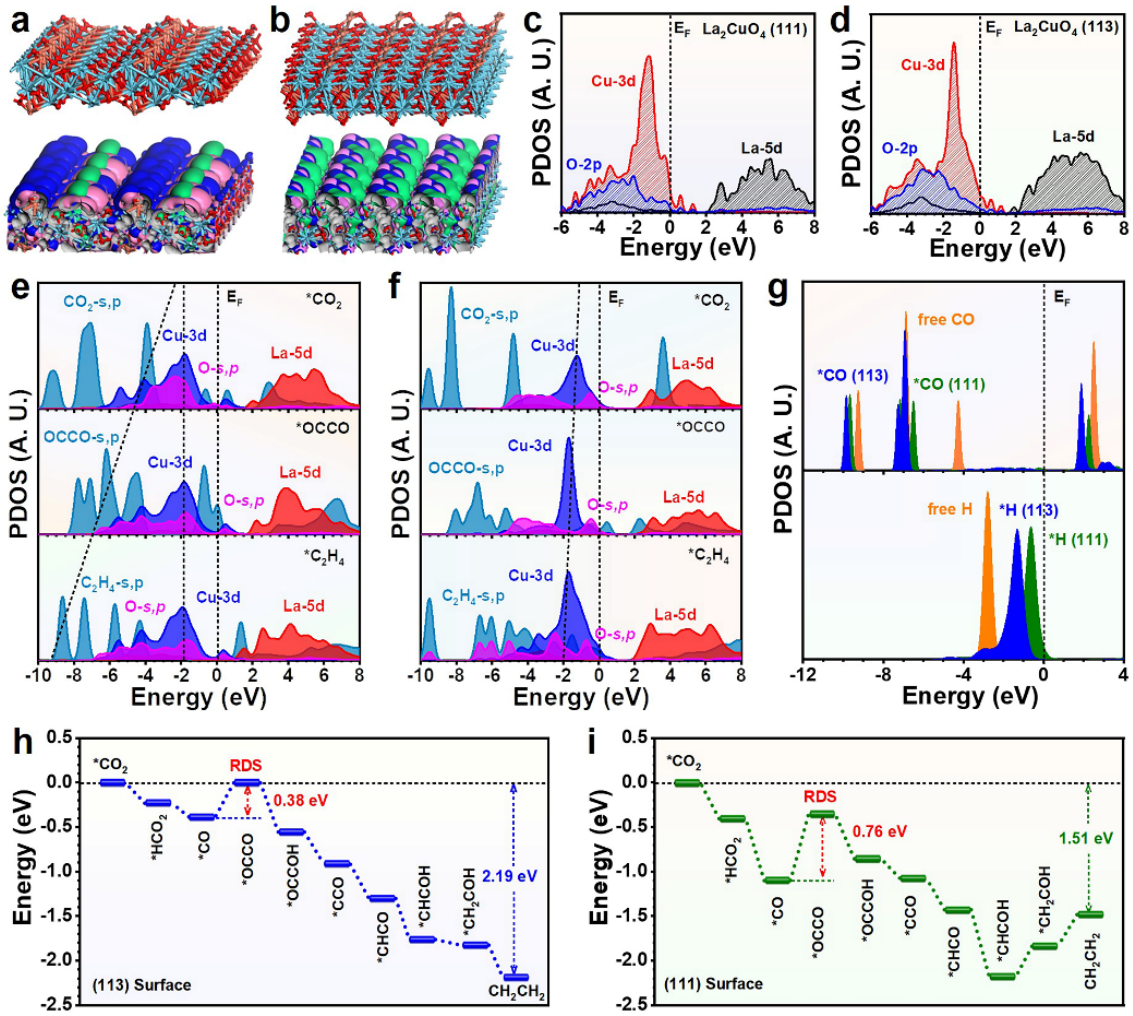

Figure 5. (a) Structural configurations and real spatial 3D orbital contour plots of (a) (113) and (b) (111) surface of La_2CuO_4. Blue balls= La, Orange balls= Cu and Red balls = O. PDOSs of (c) (113) and (d) (111) surface of La_2CuO_4. PDOSs of key adsorbates of the C_2 route on (e) (113) and (f) (111) surface of La_2CuO_4. (g) PDOSs of CO* and H* adsorbates on (113) and (111) surface of La_2CuO_4. (h) The energetic pathway of CO_2 reduction to C_2H_4 on (113) surfaces. (i) The energetic pathway of CO_2 reduction to C_2H_4 on (111) surfaces.

We also compare the energetic reaction trend of CO_2 reduction on both surfaces. For the (113) surface, the rate-determining step (RDS) is the C-C coupling, which is the key step for the C_2 route in CO_2 reduction. The RDS shows a slight barrier of 0.38 eV. The strain induced within TBs in La_2CuO_4 NBs largely promotes the C-C couplings of the C_2 route. A strong reaction trend is noted for (113) surface by releasing overall energy of 2.19 eV, supporting the high FE of C_2H_4 formation (**Figure 5h**). On the

contrary, we notice a much larger energy barrier of RDS (0.76 eV) for (111) surface, which is induced by the overbinding of CO*. The two times higher RDS barrier leads to the distinct selectivity of the surface, which is trapped in the formation of the C_1 product of CO. Moreover, the overall reaction energy also supports the enhanced selectivity of (113) surface on the C_2 product of C_2H_4 (**Figure 5i**). Therefore, the different selectivity of La_2CuO_4 NBs, La_2CuO_4 NRs, and bulk La_2CuO_4 is attributed to the intrinsic electroactivity of the different surfaces. For La_2CuO_4 NBs with high FE of C_2H_4, the main contribution comes from both highly electroactive (113) surfaces and the facilitation of strain-induced between TBs. Meanwhile, the La_2CuO_4 NRs shows less selectivity to the C_2 product due to the less electroactive (111) surfaces. The minute amount of C_2 product is achieved by the strain of GBs, which lowers the energy barrier of RDS and increases the electron transfer efficiency. For bulk La_2CuO_4, the lack of strain cannot overcome the RDS barrier of C-C coupling in C_2 route, which leads to the formation of CO and H_2 in the product. Therefore, our calculations have confirmed the contributions of both high index facets and the twin boundary to the superior performance of CO_2RR in this work.

Conclusion. In summary, we have successfully created a series of La_2CuO_4 perovskites with controlled GBs as efficient electrocatalysts for CO_2RR by simply changing the heating rate in the calcination process. The optimized La_2CuO_4 NBs exhibit a high FE towards C_2H_4 (60%) while the bulk La_2CuO_4 shows a FE_{CO} up to 91%. TPD results reveal that the strong adsorption affinity for CO intermediates improves the selectivity towards C_2 product. XAS results display that the TBs in La_2CuO_4 NBs generate strain leading to increased Cu-O and Cu-La bond length and produce coordinatively unsaturated environment to enhance the adsorption of the intermediate for improved FE_{C2H4}. DFT calculations confirm that the high performance of CO_2RR on La_2CuO_4 NBs is attributed to the high activity of (113) surfaces for electron transfer and the efficient C-C coupling facilitated by the induced strain in TBs. The combination of active

surface and strain determines the selectivity and efficiency of CO_2RR. The present work highlights the important role of grain boundary engineering in the design of high-performance CO_2RR electrocatalysts for hydrocarbon production and beyond.

ASSOCIATED CONTENT

Supporting Information. Experimental details and data. Figures S1-S29 & Table S1-S4. This material is available free of charge *via* the Internet at http://pubs.acs.org.

Corresponding Author

hxq006@xmu.edu.cn

Author Contributions

X.H. conceived and supervised the research. X.H. and J.W. designed the experiments. X.H., J.W., C.C., L.L., Q.S. and L.Z. performed most of the experiments and data analysis. X.H., J.W., C.C., L.L., Q.S., and L.Z. participated in various aspects of the experiments and discussions. B.H. performed the DFT simulations. X.H., J.W., C.C. and B.H. wrote the paper. All authors discussed the results and commented on the manuscript. J.W., C.C., and B.H. contributed equally to this work.

ACKNOWLEDGMENT

This work was financially supported by the Ministry of Science and Technology of China (2016YFA0204100, 2017YFA0208200), Young Thousand Talented Program, the Natural Science Foundation of Jiangsu Higher Education Institutions (17KJB150032), the project of scientific and technologic infrastructure of Suzhou (SZS201708), the Priority Academic Program Development of

Jiangsu Higher Education Institutions (PAPD), and start-up support from Xiamen University.

References

(1) Dinh, C. T.; Burdyny, T.; Kibria, M. G.; Seifitokaldani, A.; García de Arquer, C. M. Gabardo. F. P.; Kiani, A.; Edwards, J. P.; Luna, P. D.; Bushuyev, O. S.; Zou, C.; Quintero-Bermudez, R.; Pang, Y.; Sinton, D.; Sargent, E. H. CO_2 electroreduction to ethylene via hydroxide-mediated copper catalysis at an abrupt interface. *Science* **2018**, *360,* 783-787.

(2) He, L.; Sun, X.; Zhang, H.; Shao, F. G-quadruplex nanowires to direct the efficiency and selectivity of electrocatalytic CO_2 reduction. *Angew. Chem. Int. Ed.* **2018**, *57,* 12453-12457.

(3) Wang, J.; Ji, Y.; Shao, Q.; Yin, R.; Guo, J.; Li, Y.; Huang, X. Phase and structure modulating of bimetallic CuSn nanowires boosts electrocatalytic conversion of CO_2. *Nano Energy* **2019**, *59,* 138-145.

(4) Lu, X.; Wu, Y.; Yuan, X.; Wang, H. An integrated CO_2 electrolyzer and formate fuel cell enabled by a reversibly restructuring Pb-Pd bimetallic catalyst. *Angew. Chem. Int. Ed.* **2019**, *58,* 4031-4035.

(5) Tao, Z.; Wu, Z.; Yuan, X.; Wu, Y.; Wang, H. Copper-gold interactions enhancing formate production from electrochemical CO_2 reduction. *ACS Catal.* **2019**, *9*, 10894-10898.

(6) Dou, S.; Song, J.; Xi, S.; Du, Y.; Wang, J.; Huang, Z. F.; Xu, Z. J.; Wang, X. Boosting electrochemical CO_2 reduction on metal-organic frameworks via ligand doping. *Angew. Chem. Int. Ed.* **2019**, *131*, 4081-4085.

(7) Wu, Y.; Jiang, Z.; Lu, X.; Liang, Y.; Wang, H. Domino electroreduction of CO_2 to methanol on a molecular catalyst. *Nature* **2019**, *575*, 639-642.

(8) Jiang, K.; Siahrostami, S.; Zheng, T.; Hu, Y.; Hwang, S.; Stavitski, E.; Peng, Y.; Dynes, J.; Gangisetty, M.; Su, D.; Attenkofer, K.; Wang, H. Isolated Ni single atoms in graphene nanosheets for high-performance CO_2 reduction. *Energy Environ. Sci.* **2018**, *11*, 893-903.

(9) Jiang, K.; Wang, H.; Cai, W. B.; Wang, H. Li electrochemical tuning of metal oxide for highly selective CO_2 reduction. *ACS Nano* **2017**, *11*, 6451-6458.

(10) Choi, C.; Cheng, T.; Espinosa, M. F.; Fei, H.; Duan, X.; Goddard III, W. A.; Huang, Y.; A highly active

star decahedron Cu nanocatalyst for hydrocarbon production at low overpotentials. *Adv. Mater.* **2019**, *31*, 1805405.

(11) Wang, J.; Gan, L.; Zhang, Q.; Reddu, V.; Peng, Y.; Liu, Z.; Xia, X.; Wang, C.; Wang, X. A water-soluble Cu complex as molecular catalyst for electrocatalytic CO_2 reduction on graphene-based electrodes. *Adv. Energy Mater.* **2019**, *9*, 1803151.

(12) Yoshio, H.; Katsuhei, K.; Shin, S. Production of CO and CH_4 in electrochemical reduction of CO_2 at metal electrodes in aqueous hydrogencarbonate solution. *Chem. Lett.* **1985**, *14*, 1659-1698.

(13) Weng, Z.; Zhang, X.; Wu, Y.; Huo, S.; Jiang, J.; Liu, W.; He, G.; Liang, Y.; Wang, H. Self-cleaning catalyst electrodes for stabilized CO_2 reduction to hydrocarbons. *Angew. Chem. Int. Ed.* **2017**, *56*, 13135-13139.

(14) Jiang, K.; Sandberg, R. B.; Akey, A. J.; Liu, X.; Bell, D. C.; Nørskove, J. K.; Chan, K.; Wang, H. Metal ion cycling of Cu foil for selective C-C coupling in electrochemical CO_2 reduction. *Nat. Catal.* **2018**, *1*, 111-119.

(15) Vasileff, A.; Zhu, Y.; Zhi, X.; Zhao, Y.; Ge, L.; Chen, H. M.; Zheng, Y.; Qiao, S. Z.; Electrochemical reduction of CO_2 to ethane through stabilization of an ethoxy intermediate. *Angew. Chem. Int. Ed.* DOI: org/10.1002/ange.202004846.

(16) Luc, W.; Fu, X.; Shi, J.; Lv, J. J.; Jouny, M.; Ko, B. H.; Xu, Y.; Tu, Q.; Hu, X.; Wu, J.; Yue, Q.; Liu, Y.; Jiao, F.; Kang, Y. Two-dimensional copper nanosheets for electrochemical reduction of carbon monoxide to acetate. *Nat. Catal.* **2019**, *2*, 423-430.

(17) Li, Q.; Fu, J.; Zhu, W.; Chen, Z.; Shen, B.; Wu, L.; Xi, Z.; Wang, T.; Lu, G.; Zhu, J. J.; Sun, S. Tuning Sn-catalysis for electrochemical reduction of CO_2 to CO via the core/shell Cu/SnO_2 structure. *J. Am. Chem. Soc.* **2017**, *139*, 4290-4293.

(18) Wang, P.; Qiao, M.; Shao, Q.; Pi, Y.; Zhu, X.; Li, Y.; Huang, X. Phase and structure engineering of copper tin heterostructures for efficient electrochemical carbon dioxide reduction. *Nat. Commun.* **2018**, *9*, 4933.

(19) Zhu, S.; Jiang, B.; Cai, W. B.; Shao, M. Direct observation on reaction intermediates and the role of bicarbonate anions in CO_2 electrochemical reduction reaction on Cu surfaces. *J. Am. Chem. Soc.* **2017**, *139*, 15664-15667.

(20) Hwang, J.; Rao, R. R.; Giordano, L.; Katayama, Y.; Yu, Y.; Shao-Horn, Y. Perovskites in catalysis and electrocatalysis. *Science* **2017**, *358*, 751-756.

(21) Chen, Y.; Li, H.; Wang, J.; Du, Y.; Xi, S.; Sun, Y.; Sherburne, M.; Ager III, J. W.; Fisher, A. C.; Xu, Z. J. Exceptionally active iridium evolved from a pseudocubic perovskite for oxygen evolution in acid. *Nat. Commun.* **2019**, *10*, 572.

(22) Kim, C. H.; Qi, G.; Dahlberg, K.; Li, W. Strontium-doped perovskites rival platinum catalysts for treating NO_x in simulated diesel exhaust. *Science* **2010**, *327*, 1624-1627.

(23) Chan, K. S.; Ma, J.; Jaenicke, S.; Chuah, G. K.; Lee, J. Y. Catalytic carbon monoxide oxidation over strontium, cerium and copper-substituted lanthanum manganates and cobaltates. *A Appl. Catal. A Gen.* **1994**, *107*, 201-227.

(24) Zhou, S.; Miao, X.; Zhao, X.; Ma, C.; Qiu, Y.; Hu, Z.; Zhao, J.; Shi, L.; Zeng, J. Engineering electrocatalytic activity in nanosized perovskite cobaltite through surface spin-state transition. *Nat. Commun.* **2016**, *7*, 11510.

(25) Wang, H.; Wang, J.; Pi, Y.; Shao, Q.; Tan, Y.; Huang, X. Double perovskite $LaFe_xNi_{1-x}O_3$ nanorods enable efficient oxygen evolution electrocatalysis. *Angew. Chem. Int. Ed.* **2018**, *58*, 2316-2320.

(26) Hwang, J.; Akkiraju, K.; Corchado-García, J.; Shao-Horn, Y. A perovskite electronic structure descriptor for electrochemical CO_2 reduction and the competing H_2 evolution reaction. *J. Phys. Chem. C* **2019**, *123*, 24469-24476.

(27) Pi, Y.; Guo, J.; Shao, Q.; Huang, X. All-inorganic $SrSnO_3$ perovskite nanowires for efficient CO_2 electroreduction. *Nano Energy* **2019**, *62*, 861-868.

(28) Luo, W.; Hu, X.; Sun, Y.; Huang, Y. Electrospun porous $ZnCo_2O_4$ nanotubes as a high-performance anode

material for lithium-ion batteries. *J. Mater. Chem.* **2012**, *22*, 8916-8921.

(29) Koczkur, K. M.; Mourdikoudis, S.; Polavarapu, L.; Skrabalak, S. E. Polyvinylpyrrolidone (PVP) in nanoparticle synthesis. *Dalton Trans.* **2015***, 44*, 17883-17905.

(30) Lv, H.; Lin, L.; Zhang, X.; Gao, D.; Song, Y.; Zhou, Y.; Liu, Q.; Wang, G.; Bao, X. In situ exsolved $FeNi_3$ nanoparticles on nickel doped $Sr_2Fe_{1.5}Mo_{0.5}O_{6-\delta}$ perovskite for efficient electrochemical CO_2 reduction reaction. *J. Mater. Chem. A* **2019**, *7*, 11967-11975.

(31) Yin, Z.; Gao, D.; Yao, S.; Zhao, B.; Cai, F.; Lin, L.; Tang, P.; Zhai, P.; Wang, G.; Ma, D.; Bao, X. Highly selective palladium-copper bimetallic electrocatalysts for the electrochemical reduction of CO_2 to CO. *Nano Energy* **2016**, *27*, 35-43.

TOC graphic

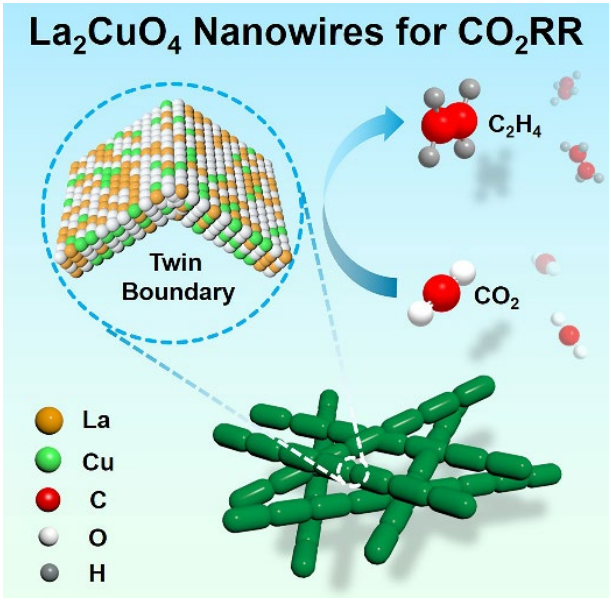
La2CuO4 Nanowires for CO2RR
C2H4
CO2
Twin
Boundary
La
Cu
C
O
H